Journal of Ultrafine Grained and Nanostructured Materials
https://jufgnsm.ut.ac.ir
Vol. 58, No.2, June 2025, pp. 132-142
Print ISSN: 2423-6845 Online ISSN: 2423-6837
DOI: 10.22059/jufgnsm.2025.02.01

Nanostructured spinel ferrites $NiFe_2O_4$ and $CoFe_2O_4$: influence of cation substitution on crystal structure, surface stability, and magnetic behavior

S. Khanahmadi, H. R. Madaah Hosseini*, G. Pircheraghi

[1]P Department of Materials Science and Engineering, Sharif University of Technology (SUT), Tehran, Iran

Recieved: 12 November 2025; Accepted: 3 December 2025

**Corresponding author, E-mail:* Madaah@sharif.edu

ABSTRACT

Nanostructured spinel ferrites $NiFe_2O_4$ and $CoFe_2O_4$ were synthesized via a chemical co-precipitation route under identical conditions to enable a direct comparison of their cation-dependent structure, colloidal stability, and magnetic behavior. X-ray diffraction (XRD) confirmed the formation of single-phase cubic spinels with nanoscale crystallites. The broad peaks reflected nanoscale crystallites; however, field-emission scanning electron microscopy (FESEM) revealed agglomerated nanoparticles with an average particle size of ~100 nm. Dynamic light scattering (DLS) revealed hydrodynamic diameters of 185 nm for $CoFe_2O_4$ and 171 nm for $NiFe_2O_4$, while the zeta potentials of -29 mV and -37 mV indicated moderate and higher colloidal stability, respectively. Magnetic measurements demonstrated a clear contrast between the two ferrites: $CoFe_2O_4$ exhibited higher saturation magnetization (75 emu g^{-1}) and coercivity (860 Oe) than the softer $NiFe_2O_4$ (36 emu g^{-1}, 139 Oe). The corresponding squareness ratios of 0.45 and 0.22 supported the transition from hard to soft magnetic behavior with cation substitution. These findings reveal that replacing Ni^{2+} with Co^{2+} increases magnetocrystalline anisotropy and magnetic hardness while slightly lowering colloidal stability, establishing a direct link between cation type, structural order, and magnetic performance in spinel ferrite nanostructures.

Keywords: *Nanostructured spinel ferrites; $NiFe_2O_4$ and $CoFe_2O_4$ nanoparticles; Cation substitution; Chemical co-precipitation; Magnetic properties.*

1. Introduction

Spinel ferrites of the general formula MFe_2O_4 have attracted wide attention due to their high chemical stability, tunable magnetic characteristics, and compatibility with diverse applications such as sensors, microwave absorbers, data storage, and biomedical systems [1,2]. The cubic Fd3m structure allows flexible occupation of tetrahedral and octahedral sites by different metal cations, providing a rich platform to tailor superexchange interactions and magnetic anisotropy [3,4]. Among them, cobalt and nickel ferrites have gained particular interest because their distinct cationic preferences and exchange energies lead to pronounced variations in coercivity and saturation magnetization [5,6].

Various synthetic routes including sol-gel, combustion, hydrothermal, and chemical co-precipitation methods have been employed to prepare spinel ferrites [7-9]. Among these, chemical co-precipitation is considered one of the most efficient approaches owing to its simplicity, low processing temperature, and fine control over stoichiometry [10,11]. The microstructure and

resulting magnetic behavior are highly dependent on parameters such as pH, precursor chemistry, and calcination temperature [12]. In the present study, both $NiFe_2O_4$ and $CoFe_2O_4$ were synthesized using chloride precursors at pH 12 and calcined at 800 °C to ensure identical processing conditions and allow a fair comparison of cation-dependent effects.

Earlier investigations have consistently shown that $CoFe_2O_4$ possesses higher coercivity and magnetization than $NiFe_2O_4$, reflecting its hard-magnetic character, whereas $NiFe_2O_4$ behaves as a soft ferrite [13,14]. These contrasting behaviors stem from the greater magnetocrystalline anisotropy of Co^{2+} and the differing degree of cation inversion between the two ferrites [15,16]. Spectroscopic studies have further revealed that shifts in metal-oxygen stretching vibrations in the Fourier-transform infrared spectra correspond to cation redistribution between tetrahedral and octahedral sites [4,17], corroborating structural adjustments at the nanoscale.

Despite the broad literature on ferrites, most previous works focused on doped compositions or employed dissimilar synthetic routes for the two ferrites, making direct comparison difficult [18,19]. Moreover, the interplay between surface stability and magnetic parameters has been rarely addressed, even though colloidal behavior is critical for aqueous and biomedical applications. Establishing a clear correlation between synthesis conditions, cation substitution, and magnetic response remains essential for designing ferrites with predictable performance.

Therefore, in this research, $NiFe_2O_4$ and $CoFe_2O_4$ nanostructures were prepared through a controlled chemical co-precipitation process using chloride precursors at pH 12, followed by calcination at 800 °C. The aim was to systematically evaluate the influence of cation type on crystal structure, particle morphology, colloidal stability, and magnetic behavior. Structural and spectroscopic analyses using X-ray diffraction (XRD), Fourier-transform infrared spectroscopy (FTIR), field-emission scanning electron microscopy (FESEM), and dynamic light scattering (DLS), combined with magnetic measurements performed by vibrating sample magnetometry (VSM), provide comprehensive insights into how cation substitution modifies lattice order, magnetic hardness, and colloidal stability in spinel ferrite nanostructures. The comparative results are expected to clarify the process-structure-property relationships between these two technologically significant ferrites and contribute to the broader understanding of cation-controlled magnetism at the nanoscale. This study is designed to provide a side-by-side comparison of $CoFe_2O_4$ and $NiFe_2O_4$ spinel ferrites synthesized under identical conditions.

2. Experimental Details

2.1. Materials

All reagents were of analytical grade and used as received without any further purification. Ferric(III) chloride hexahydrate ($FeCl_3.6H_2O$), nickel(II) chloride hexahydrate ($NiCl_2.6H_2O$), cobalt(II) chloride hexahydrate ($CoCl_2.6H_2O$), and sodium hydroxide (NaOH) were purchased from Sigma-Aldrich with a stated purity above 99%. Double-distilled water was used throughout the synthesis as the solvent and reaction medium.

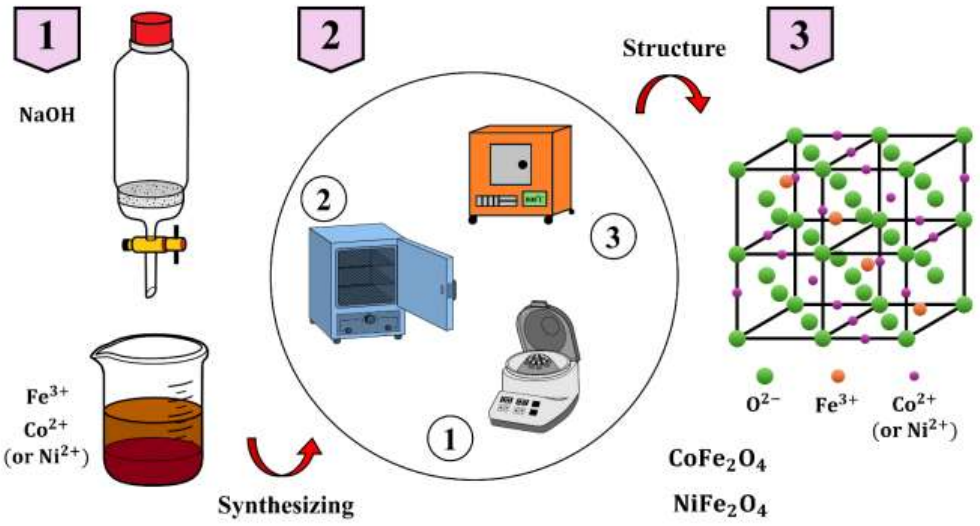

Fig. 1- Schematic illustration of the chemical co-precipitation route used for synthesizing $NiFe_2O_4$ and $CoFe_2O_4$ nanoparticles.

2.2. Synthesis method

$NiFe_2O_4$ and $CoFe_2O_4$ nanostructures were synthesized via a chemical co-precipitation route [20], as illustrated in Fig. 1. In a typical synthesis, 11.4 g of ferric(III) chloride hexahydrate ($FeCl_3.6H_2O$) and 5 g of either nickel(II) chloride hexahydrate ($NiCl_2.6H_2O$) or cobalt(II) chloride hexahydrate ($CoCl_2.6H_2O$) were separately dissolved in deionized (DI) water and then mixed under continuous stirring at room temperature to form a homogeneous solution. A 1 M sodium hydroxide (NaOH) solution was added dropwise until the pH of the mixture reached approximately 12, resulting in the formation of brown ferrite hydroxide precipitates. The precipitates were thoroughly washed three times with DI water and ethanol to remove residual ions and dried in an oven at 60 °C for 48 h. Finally, the dried powders were calcined in a muffle furnace at 800 °C for 2 h to obtain pure spinel $NiFe_2O_4$ and $CoFe_2O_4$ phases. This pH was selected to promote nearly complete co-precipitation of Ni^{2+}/Co^{2+} and Fe^{3+} hydroxides and to suppress the formation of unwanted soluble or mixed-valence byproducts. The calcination temperature of 800 °C was chosen as a compromise, being high enough to ensure full conversion to the cubic spinel phase while limiting excessive grain growth.

2.3. Characterization

The structural, morphological, and magnetic characteristics of the synthesized $NiFe_2O_4$ and $CoFe_2O_4$ nanostructures were examined using several analytical techniques. The crystal structure was identified by XRD using an X'Pert PRO diffractometer (PANalytical, Netherlands) operated at 40 kV and 40 mA with Cu Kα radiation (λ = 1.5406 Å) in the 2θ range of 5-80° and a scan step of 0.026°. The chemical bonding and functional groups were investigated through FTIR performed on a PerkinElmer Spectrum RXI spectrometer over the range 400-4000 cm^{-1}. The morphology and surface microstructure of the samples were observed using FESEM (TESCAN MIRA 3) equipped with an energy-dispersive X-ray spectroscopy (EDS) detector for elemental mapping and compositional analysis. The average particle size was further estimated from FESEM images using the ImageJ software (National Institutes of Health, USA). Particle size distribution and surface charge were determined by DLS and zeta potential measurements using a Malvern Zetasizer ZN series at room temperature. The magnetic properties were measured at room temperature using VSM (Magnetic Daneshpajoh Kashan) under an applied magnetic field of up to ±15 kOe.

3. Results and discussion

3.1. Phase and crystal structure

X-ray diffraction patterns of both $NiFe_2O_4$ and $CoFe_2O_4$ (Fig. 2 (a)) confirm a single cubic spinel phase with the Fd3m space group. The main reflections appear at approximately 2θ ≈ 18°, 30°, 35°, 37°, 43°, 54°, 57°, 63°, 71°, 74°, 75°, and 79°, which were indexed to the (111), (022), (131), (222), (040), (242), (151), (044), (062), (353), (262), and (444) planes, respectively [20]. The patterns match well with the ICDD reference cards for $CoFe_2O_4$ (96-153-3164) and $NiFe_2O_4$ (96-591-0065), and no additional peaks were detected, indicating phase purity. The peak positions of the two ferrites nearly overlap, consistent with their identical crystal

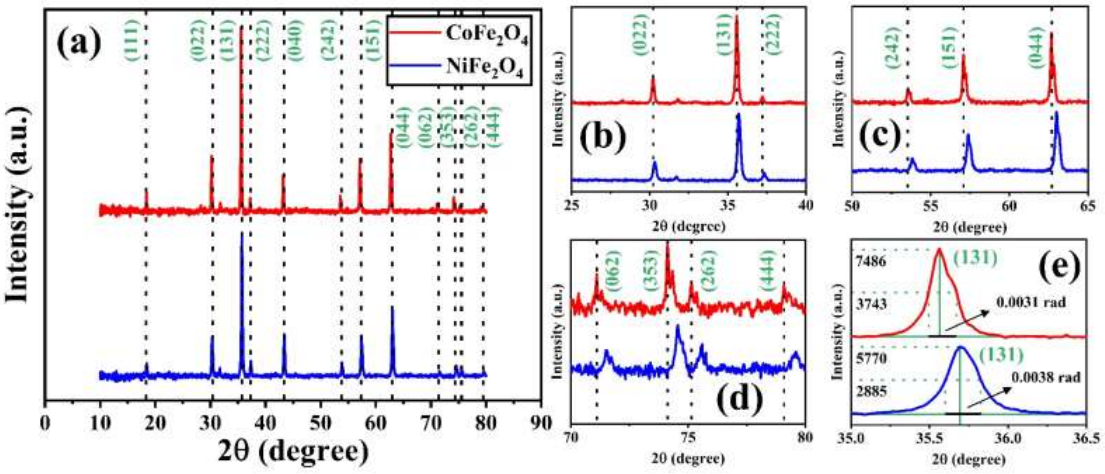

Fig. 2- . (a) XRD patterns of $NiFe_2O_4$ and $CoFe_2O_4$ confirming a single-phase cubic spinel (Fd3m); (b-d) peak shifts of $NiFe_2O_4$ toward higher 2θ values due to smaller Ni^{2+} ionic radius; (e) broader (131) peak for $NiFe_2O_4$ indicating smaller crystallite size.

symmetry and the close ionic radii of Co^{2+} and Ni^{2+}, so no noticeable 2θ shift is expected between them (Fig. 2 (b-d)). The FCC-type oxygen sublattice and the ordered spinel framework are thus verified for both compositions. Calculated d-spacings and indices agree with the reference files within experimental uncertainty.

The crystallite size was determined from the main (311) diffraction peak using the Debye-Scherrer equation (Eq. 1):

$$D = \frac{K\lambda}{\beta \cos(\theta)} \quad (1)$$

where K = 0.9 is the shape factor, λ = 1.5406 Å is the Cu Kα wavelength, β is the FWHM of the (131) peak corrected for instrumental broadening and expressed in radians, and θ is the Bragg angle. The (131) peak profile was fitted (Fig. 2 (e)), and the instrumental contribution was subtracted using a standard reference. The calculated crystallite sizes for $NiFe_2O_4$ and $CoFe_2O_4$ were 38 nm and 47 nm, respectively.

3.2. Metal-oxygen bonding and vibrational band features

The FTIR spectra in the 400-4000 cm^{-1} range exhibit the two characteristic spinel absorption bands (Fig. 3 (a)). The tetrahedral metal-oxygen stretching appears at ≈ 603 cm^{-1} for $NiFe_2O_4$ and ≈ 590 cm^{-1} for $CoFe_2O_4$, while the octahedral Fe-O stretching is observed at ≈ 422 cm^{-1} for $NiFe_2O_4$ and ≈ 405 cm^{-1} for $CoFe_2O_4$. The higher wavenumbers in the nickel ferrite are consistent with the smaller ionic radius of Ni^{2+} and the resulting stronger metal-oxygen bonds (Fig. 3 (b)) [21]. This shift can be attributed to shorter Ni-O bond lengths and larger force constants in $NiFe_2O_4$, which enhance the vibration frequency of the metal-oxygen lattice. In contrast, the larger ionic radius of Co^{2+} in $CoFe_2O_4$ leads to weaker bonding and hence lower vibrational energy. Additional features at 3435 cm^{-1} and 1611 cm^{-1} arise from O-H stretching and H-O-H bending of adsorbed water, and the band at 2355 cm^{-1} is attributed to atmospheric CO_2. The absence of extra absorption bands supports the formation of the spinel structure in both samples without detectable secondary phases [22,23].

3.3. Microstructure and elemental homogeneity

The microstructural morphology of the synthesized $NiFe_2O_4$ and $CoFe_2O_4$ samples is shown in Fig. 4(a, b). Both ferrites exhibit closely packed nanoparticles with irregular polyhedral shapes, typical of spinel ferrites prepared via co-precipitation [24]. The grains form dense agglomerates with intergranular voids, suggesting partial coalescence during calcination at 800 °C. No secondary or impurity phase is observed, indicating that the calcination process preserved single-phase integrity. The particle size distribution obtained from ImageJ analysis (Fig. 4(c)) reveals an average size of approximately 89 nm for $NiFe_2O_4$ and 114 nm for $CoFe_2O_4$, confirming nanoscale morphology consistent with the crystallite dimensions estimated from XRD. Because FESEM was conducted on dried and heat-treated powders, some degree of aggregation is expected; accordingly, FESEM mainly provides particle/grain-level morphology. Consistent with this, the FESEM-observed particle/grain sizes (~89-114

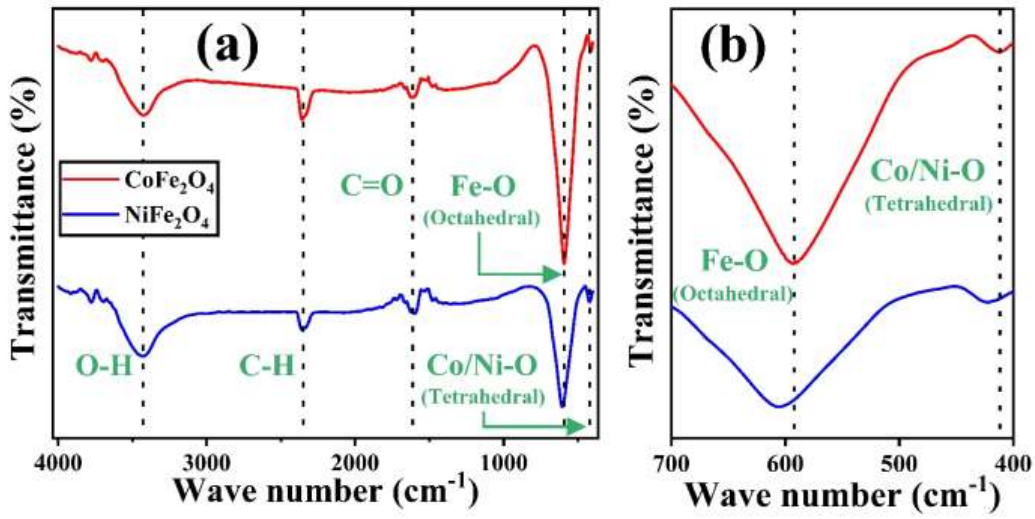

Fig. 3- FTIR spectra of $NiFe_2O_4$ and $CoFe_2O_4$ showing the spinel metal-oxygen vibrations.

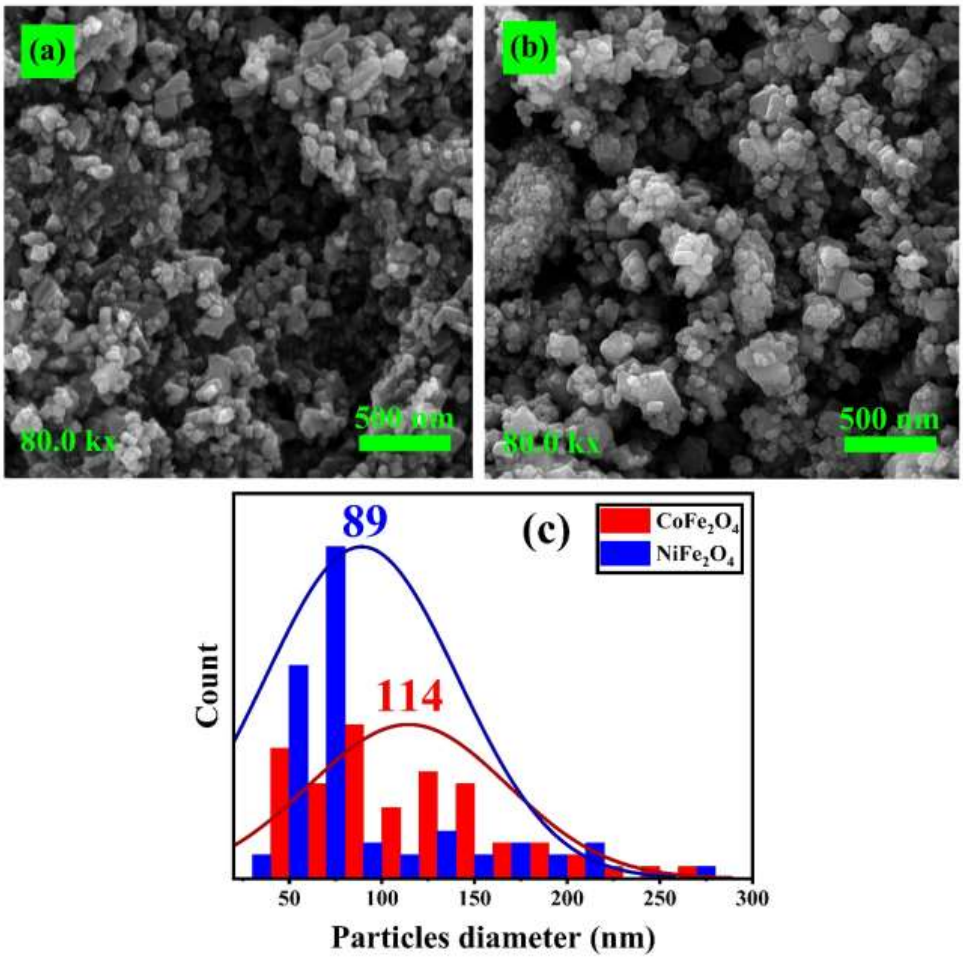

Fig. 4- FESEM images of (a) $NiFe_2O_4$ and (b) $CoFe_2O_4$ nanoparticles recorded at a magnification of 80.0 kx, showing densely agglomerated polyhedral grains with nanoscale morphology and (c) particle size distribution histograms obtained from Image.

nm) are larger than the XRD crystallite sizes (~38-47 nm), indicating that the imaged particles likely comprise multiple crystallites and/or experienced partial coalescence during calcination, while the primary crystallite size is more appropriately inferred from XRD.

The corresponding EDS spectra and elemental mapping images (Fig. 5) confirm the presence of Fe, O, and the respective divalent cations (Ni or Co) with no detectable extraneous elements. The homogeneous distribution of all constituent atoms across the scanned regions verifies complete cation incorporation into the spinel lattice and the absence of compositional segregation at the nanoscale.

3.4. Dispersion and colloidal stability in aqueous media

The particle size distribution of the synthesized ferrite nanoparticles was evaluated using dynamic light scattering (Fig. 6). Both $NiFe_2O_4$ and $CoFe_2O_4$ exhibit single, narrow peaks, indicating a uniform particle dispersion. The hydrodynamic diameters were determined to be 171 nm for $NiFe_2O_4$ and 185 nm for $CoFe_2O_4$. The slightly larger hydrodynamic diameters compared with the sizes estimated from XRD and FESEM are expected, since DLS measures solvated (hydrated) entities in the liquid phase rather than the dry particle/grain size. Differences between DLS- and microscopy-

derived sizes, as well as their interpretation, have been discussed in comparative particle-size characterization studies using SEM and DLS [25].

The schematic illustration in Fig. 7(a) depicts the electrical double-layer model that defines the zeta potential (ζ), showing the Stern layer, slipping plane, and potential decay as a function of distance from the particle surface. This conceptual diagram clarifies the physical meaning of ζ potential, representing the electrostatic potential at the slipping plane between stationary and mobile ions. The experimental values presented in Fig. 7(b) reveal zeta potentials of -37 mV for $NiFe_2O_4$ and -29 mV for $CoFe_2O_4$. The negative values and their magnitudes above 25 mV indicate sufficient electrostatic repulsion for colloidal stability [26]. The higher absolute ζ potential of $NiFe_2O_4$ implies stronger surface charge and enhanced suspension stability compared with $CoFe_2O_4$. In aqueous dispersions, such a difference in ζ potential is reasonable because replacing Ni^{2+} with Co^{2+} modifies the local coordination environment and surface chemistry of the spinel ferrite. This change can alter the density and protonation state of surface hydroxyl groups and other adsorption sites, which directly govern the electrostatic potential at the slipping plane and thus the measured ζ values. More broadly, ferrite-based magnetic nanomaterials are known to exhibit a strong link between crystal chemistry, surface physicochemical properties, and colloidal stability, as highlighted in recent studies on ferrite photocatalysts [42].

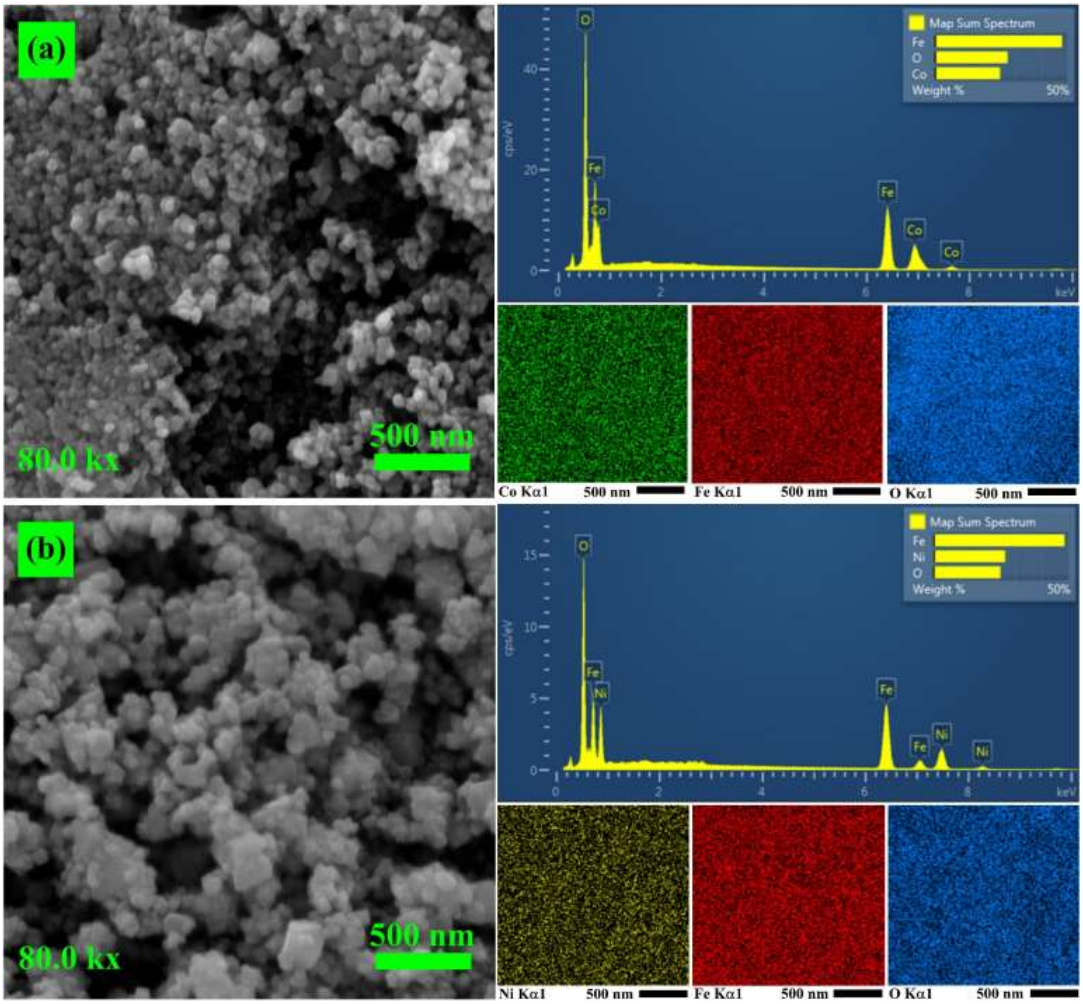

Fig. 5- EDS spectra and elemental maps of (a) $CoFe_2O_4$ and (b) $NiFe_2O_4$ confirming the presence and homogeneous distribution of Co/Ni element, Fe and O.

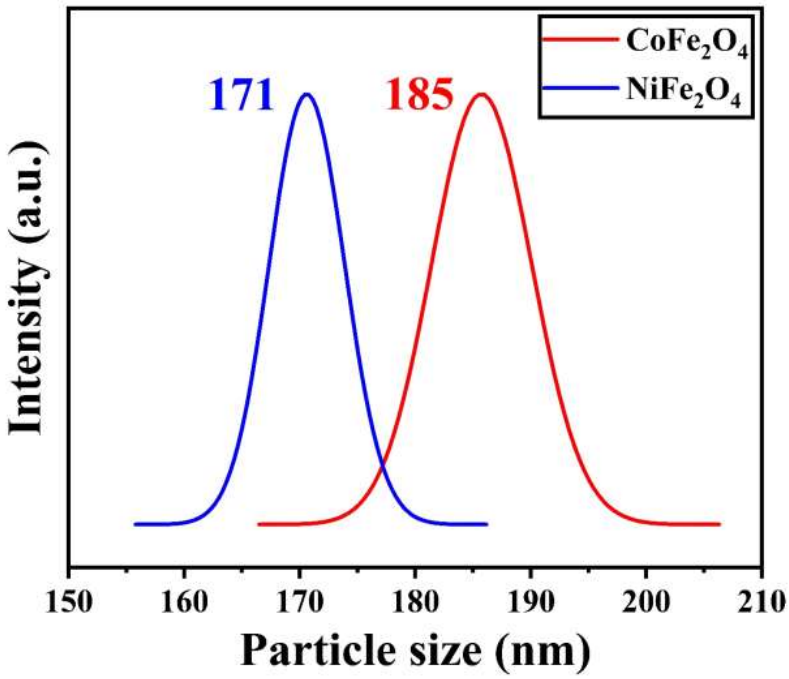

Fig. 6- Particle size distribution of $NiFe_2O_4$ and $CoFe_2O_4$ nanoparticles obtained from DLS analysis.

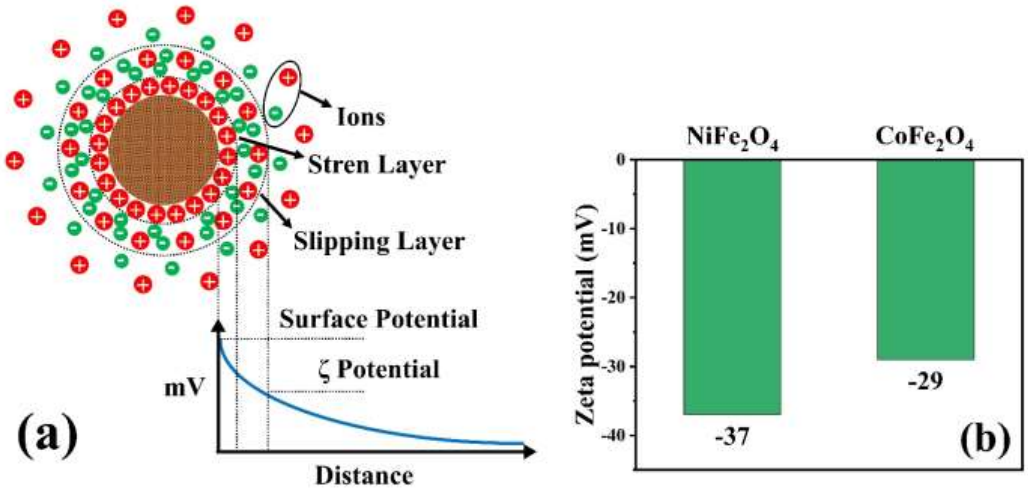

Fig. 7- (a) Schematic illustration of the electric double layer defining the zeta potential (ζ) (schematic redrawn by the authors based on Ref. [27]). (b) Measured zeta potentials of $NiFe_2O_4$ and $CoFe_2O_4$.

3.5. Magnetic response and cation-dependent hardness/softness

Magnetic hysteresis loops of the $NiFe_2O_4$ and $CoFe_2O_4$ nanoparticles were measured at room temperature under an applied magnetic field of ±15 kOe (Fig. 8). Both samples exhibit clear ferromagnetic behavior, yet their magnetic parameters show distinct variations. The extracted values of saturation magnetization (M_s), remanent magnetization (M_r), coercivity (H_c), and squareness ratio ($R_s = M_r/M_s$) are summarized in Table 1.

For $CoFe_2O_4$, the obtained M_s, M_r, H_c, and R_s values were 75 emu g^{-1}, 34 emu g^{-1}, 860 Oe, and 0.45, respectively, whereas $NiFe_2O_4$ showed lower values of 36 emu g^{-1}, 8 emu g^{-1}, 139 Oe, and 0.22. The higher M_s of $CoFe_2O_4$ originates from the intrinsically larger magnetic moment of Co^{2+} (3 μB) compared with Ni^{2+} (2 μB), as well as its stronger magnetocrystalline anisotropy, which promotes spin alignment at the octahedral (B) sites. In $CoFe_2O_4$, Co^{2+} ions predominantly occupy B sites, strengthening the Fe^{3+}-O^{2-}-Co^{2+} superexchange interactions and yielding a larger net moment (M_B-M_A) according to Néel's two-sublattice model [28-30]. In contrast, partial occupancy of Ni^{2+} ions at the tetrahedral (A) sites in $NiFe_2O_4$ reduces the overall magnetic moment.

The coercivity of $CoFe_2O_4$ (860 Oe) is roughly six times higher than that of $NiFe_2O_4$ (139 Oe), reflecting its stronger magnetic anisotropy and "semi-hard" magnetic character. This arises from the electronic configuration of Co^{2+} ($3d^7$, ^4T_1g) that preserves significant orbital angular momentum and produces a higher crystal-field anisotropy [31]. Conversely, the lower H_c of $NiFe_2O_4$ is associated with its smaller particle size and weaker anisotropy, facilitating domain-wall motion and classifying it as a "soft ferrite" [31].

The remanence ratio (M_r/M_s) also supports this distinction: $CoFe_2O_4$ exhibits a value of 0.45, characteristic of single-domain-like particles with considerable magnetic retention, while $NiFe_2O_4$ shows a smaller ratio of 0.22, indicative of multidomain behavior and lower remanence. At the nanoscale, the overall magnetic performance of these ferrites results from the interplay of crystal anisotropy, cation inversion, and surface spin disorder.

In summary, $CoFe_2O_4$ exhibits semi-hard magnetic behavior with higher M_s and H_c than $NiFe_2O_4$, whereas $NiFe_2O_4$ shows a typical soft-magnetic response with lower coercivity under identical synthesis conditions. For further context, Table 2 compares the M_s, M_r, and H_c values of the present $CoFe_2O_4$ and $NiFe_2O_4$ samples with representative literature reports for similar spinel ferrites prepared by comparable synthesis routes.

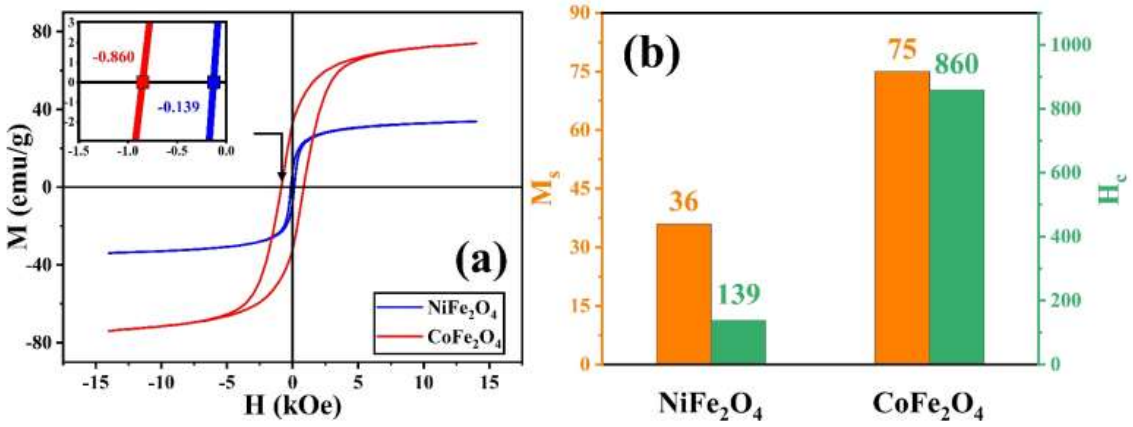

Fig. 8- (a) Magnetic hysteresis loops of $NiFe_2O_4$ and $CoFe_2O_4$nanoparticles measured at room temperature, and (b) comparison of M_s and H_c values showing higher magnetization and coercivity for $CoFe_2O_4$.

Table. 1- Magnetic parameters of $NiFe_2O_4$ and $CoFe_2O_4$ nanoparticles obtained from VSM measurements at room temperature

Spinel ferrite	M_s (emu g^{-1})	M_r (emu g^{-1})	R_s	H_c (Oe)
$CoFe_2O_4$	75	34	0.45	860
$NiFe_2O_4$	36	8	0.22	139

3.6. Correlation between structure and magnetism

The combined structural and magnetic results indicate that the magnetic contrast between $CoFe_2O_4$ and $NiFe_2O_4$ is mainly governed by cation distribution/inversion, magnetocrystalline anisotropy, and nanoscale size effects in spinel ferrites [6,15,16,30]. Although both samples crystallize in a single-phase cubic spinel (Fd3m), the divalent cation can modify the local metal-oxygen bonding environment, consistent with the observed shifts of the metal-oxygen stretching bands [21]. The higher M_s and H_c of $CoFe_2O_4$ can be rationalized by the stronger magnetocrystalline anisotropy of Co^{2+} and its preferential occupancy of octahedral (B) sites, which strengthens A-B superexchange interactions and increases the net sublattice moment (M_B-M_A) within Néel's two-sublattice framework [15,16,30]. In contrast, $NiFe_2O_4$ typically exhibits lower anisotropy and partial cation inversion, which reduces (M_B-M_A) and facilitates domain-wall motion, consistent with a softer magnetic response [15,16,30,31]. Moreover, the smaller crystallite/particle size of $NiFe_2O_4$ can enhance surface spin disorder, which may further decrease the apparent magnetization [29,30]. Therefore, under identical processing conditions, tuning the divalent cation provides an effective route to control the magnetic hardness/softness of spinel ferrite nanostructures [6,30].

4. Conclusion

$NiFe_2O_4$ and $CoFe_2O_4$ nanoparticles were successfully synthesized via a chemical co-precipitation route at pH 12 followed by calcination at 800 °C. The XRD results confirmed the formation of a single-phase cubic spinel structure with an Fd3m space group for both samples. FTIR spectra exhibited characteristic metal-oxygen stretching vibrations near 600 cm^{-1} and 420 cm^{-1}, corresponding to tetrahedral and octahedral sites, respectively. FESEM images revealed agglomerated nanosized grains with uniform elemental distribution verified by EDS mapping. DLS measurements showed hydrodynamic diameters of 185 nm for $CoFe_2O_4$ and 171 nm for $NiFe_2O_4$, while zeta potential analysis indicated higher colloidal stability for $NiFe_2O_4$ (-37 mV) compared with $CoFe_2O_4$ (-29 mV).

Magnetic characterization demonstrated a clear difference in their magnetic responses. $CoFe_2O_4$ exhibited higher saturation magnetization (M_s = 75 emu g^{-1}) and coercivity (H_c = 860 Oe) than $NiFe_2O_4$ (M_s = 36 emu g^{-1}, H_c = 139 Oe), attributed to the stronger magnetocrystalline anisotropy and exchange interactions of Co^{2+} ions. The smaller particle size and partial cation inversion in $NiFe_2O_4$ led to reduced magnetic moments and softer ferromagnetic behavior. These findings confirm that the magnetic performance of spinel ferrites can be effectively tailored by modifying the type of divalent cation while maintaining identical synthesis conditions.

Table. 2- Comparison of composition, synthesis method, and M_s, M_r, and H_c values for selected spinel ferrites analogous to the present work

Composition	Synthesis method	M_s(emu g^{-1})	M_r(emu g^{-1})	H_c(Oe)	Ref.
$CoFe_2O_4$	Sol-gel	73.7	29.1	973.5	[32]
$NiFe_2O_4$		62.7	14.5	257.0	[33]
$Cu_{0.25}Mn_{0.75}Fe_2O_4$	Sol-gel auto-combustion	32.4	18.9	0.3	[34]
$Cu_{0.25}Mg_{0.75}Fe_2O_4$		40.1	21.3	0.4	
$Cu_{0.25}Ni_{0.75}Fe_2O_4$		47.1	24.8	1.6	
$Cu_{0.25}Co_{0.75}Fe_2O_4$		59.0	34.4	3.1	
$NiFe_2O_4$	Self-combustion	6.7	1.0	159.0	[35]
$NiFe_2O_4$		37.7	6.9	114.0	
$NiFe_2O_4$	Co-precipitation /thermal decomposition	29.1	-	58.3	[36]
$NiFe_2O_4$	Co-precipitation	33.7	6.3	81.0	[37]
$CoFe_2O_4$		61.2	15.7	275.0	
$CoFe_2O_4$		69.0	30.1	302.9	[38]
$NiFe_2O_4$		47.6	13.6	500.1	[39]
$NiFe_2O_4$		30.5	6.0	134.0	
$Mn_{0.05}Ni_{0.95}Fe_2O_4$		31.8	6.6	112.0	[40]
$Zn_{0.05}Ni_{0.95}Fe_2O_4$		36.3	7.1	133.0	
$Co_{0.5}Mn_{0.5}Fe_2O_4$		85.3	15.6	229.0	[41]
$CoFe_2O_4$	Co-precipitation	75.0	34.0	860.0	This
$NiFe_2O_4$		36.0	8.0	139.0	work

References

1. Salih SJ, Mahmood WM. Review on magnetic spinel ferrite (MFe_2O_4) nanoparticles: From synthesis to application. Heliyon. 2023;9(6).
2. Ahmad SI. A review on synthesis and magnetic hyperthermia application of spinel nano ferrite. Journal of Umm Al-Qura University for Applied Sciences. 2025;1-45.
3. Hao A, Ning X. Recent advances in spinel ferrite-based thin films: synthesis, performances, applications, and beyond. Frontiers in Materials. 2021;8:718869.
4. Harada M, Kuwa M, Sato R, Teranishi T, Takahashi M, Maenosono S. Cation distribution in monodispersed MFe_2O_4 (M= Mn, Fe, Co, Ni, and Zn) nanoparticles investigated by X-ray absorption fine structure spectroscopy: implications for magnetic data storage, catalysts, sensors, and ferrofluids. ACS Applied Nano Materials. 2020;3(8):8389-402.
5. Wang W, Ding Z, Zhao X, Wu S, Li F, Yue M, Liu JP. Microstructure and magnetic properties of MFe_2O_4 (M= Co, Ni, and Mn) ferrite nanocrystals prepared using colloid mill and hydrothermal method. Journal of Applied Physics. 2015;117(17).
6. Sharma K, Calmels L, Li D, Barbier A, Arras R. Influence of the cation distribution, atomic substitution, and atomic vacancies on the physical properties of $CoFe_2O_4$ and $NiFe_2O_4$ spinel ferrites. Physical Review Materials. 2022;6(12):124402.
7. Kurian M, Thankachan S, Nair DS, EK A, Babu A, Thomas A, Krishna KT B. Structural, magnetic, and acidic properties of cobalt ferrite nanoparticles synthesised by wet chemical methods. Journal of Advanced Ceramics. 2015;4(3):199-205.
8. Chandekar KV, Yadav SP, Chinke S, Shkir M. Impact of Co-doped $NiFe_2O_4$ ($Co_xNi_{1-x}Fe_2O_4$) nanostructures prepared by co-precipitation route on the structural, morphological, surface, and magnetic properties. Journal of Alloys and Compounds. 2023;966:171556.
9. Darandale S, Hase D, Mane K, Khedkar J, Murade R, Dichayal S, Murade V. Synthesis of Spinel Ferrites and Their Composites: A Comprehensive Review on Synthesis Methods, Characterization Techniques, and Photocatalytic Applications. Journal of Chemical Reviews. 2025;7:216.
10. Nejati K, Zabihi R. Preparation and magnetic properties of nano size nickel ferrite particles using hydrothermal method. Chemistry Central Journal. 2012;6(1):23.
11. Mahhouti Z, El Moussaoui H, Mahfoud T, Hamedoun M, El Marssi M, Lahmar A, El Kenz A, Benyoussef A. Chemical synthesis and magnetic properties of monodisperse cobalt ferrite nanoparticles. Journal of Materials Science: Materials in Electronics. 2019;30(16):14913-22.
12. Kumar RJ, Khan TF, Uppara N, Orugu N, Rekha E. Structural and optical study of $CoFe_2O_4$, $NiFe_2O_4$ nanoparticles synthesized via hydrothermal synthesis. GIS Science Journal. 2021;8(4):83-94.
13. Sattar AA, El-Sayed HM, ALsuqia I. Structural and magnetic properties of $CoFe_2O_4/NiFe_2O_4$ core/shell nanocomposite prepared by the hydrothermal method. Journal of Magnetism and Magnetic Materials. 2015;395:89-96.
14. Rekha K, Vizhi RE. Exploring the structural, magnetic and magnetothermal properties of $(CoFe_2O_4)_x/(Ni_{0.8}Zn_{0.2}Fe_2O_4)_{1-x}$ nanocomposite ferrites. Results in Physics. 2023;44:106139.
15. Andersen HL, Saura-Múzquiz M, Granados-Miralles C, Klemmt R, Bøjesen ED, Christensen M. Crystal/magnetic structure and cation inversion in hydrothermally synthesized $MnFe_2O_4$, $CoFe_2O_4$, $NiFe_2O_4$, and $ZnFe_2O_4$ nanoparticles: a neutron powder diffraction study. CrystEngComm. 2025;27(6):850-64.
16. Mills PD. Magnetic and structural properties of $CoFe_2O_4$ and $NiFe_2O_4$ thin films and heterostructures. PhD Thesis. University of York; 2022.
17. Sen SK, Babu MM, Paul TC, Hossain MS, Hossain M, Dutta S, Hasan MR, Hossain MN, Matin MA, Hakim MA, Bala P. Gamma irradiated nanostructured $NiFe_2O_4$: effect of γ-photon on morphological, structural, optical, and magnetic properties. AIP Advances. 2021;11(7).
18. Khanahmadi S, Masoudpanah SM. Preparation and microwave absorption properties of $CoFe_2O_4/NiCo_2O_4$ composite powders. Ceramics International. 2024;50(6):9779-88.
19. Khanahmadi S, Masoudpanah SM. In-situ synthesis of NiCo/(Ni, Co)O/(Ni, Co)Fe_2O_4 composite as high-performance microwave absorber. Journal of Materials Research and Technology. 2023;22:585-95.
20. Roy P, Hoque SM, Akter S, Liba SI, Choudhury S. Study on the chemical co-precipitation synthesized $CoFe_2O_4$ nanoparticle for magnetocaloric performance in the vicinity of superparamagnetic blocking temperature. Heliyon. 2024;10(14).
21. Jia H, Horton M, Wang Y, Zhang S, Persson KA, Meng S, Liu M. Persona of transition metal ions in solids: A statistical learning on local structures of transition metal oxides. Advanced Science. 2022;9(27):2202756.
22. Mesbahinia A, Almasi-Kashi M, Ghasemi A, Ramezani A. First order reversal curve analysis of cobalt-nickel ferrite. Journal of Magnetism and Magnetic Materials. 2019;473:161-8.
23. Sivakumar P, Ramesh R, Ramanand A, Ponnusamy S, Muthamizhchelvan C. Synthesis and characterization of $NiFe_2O_4$ nanoparticles and nanorods. Journal of Alloys and Compounds. 2013;563:6-11.
24. Rotjanasuworapong K, Lerdwijitjarud W, Sirivat A. Synthesis and characterization of $Fe_{0.8}Mn_{0.2}Fe_2O_4$ ferrite nanoparticle with high saturation magnetization via the surfactant assisted co-precipitation. Nanomaterials. 2021;11(4):876.
25. de la Calle I, Soto-Gómez D, Pérez-Rodríguez P, López-Periago JE. Particle size characterization of sepia ink eumelanin biopolymers by SEM, DLS, and AF4-MALLS: a comparative study. Food Analytical Methods. 2019;12(5):1140-51.
26. Bhattacharjee S. DLS and zeta potential–what they are and what they are not?. Journal of controlled release. 2016;235:337-51.
27. Mohd TA, Jaafar MZ, Rasol AA, Hamid MF. Measurement of streaming potential in downhole application: An insight for enhanced oil recovery monitoring. MATEC Web of Conferences. 9th International UNIMAS STEM Engineering Conference (ENCON 2016); 2016 Oct 26–28; Sarawak, Malaysia.
28. Kooti M, Sedeh AN. Synthesis and characterization of $NiFe_2O_4$ magnetic nanoparticles by combustion method. Journal of Materials Science & Technology. 2013;29(1):34-8.
29. Majid F, Rauf J, Ata S, Bibi I, Malik A, Ibrahim SM, Ali A, Iqbal M. Synthesis and characterization of $NiFe_2O_4$ ferrite: Sol–gel and hydrothermal synthesis routes effect on magnetic, structural and dielectric characteristics. Materials Chemistry and Physics. 2021;258:123888.
30. Goldman A. Modern ferrite technology. 2nd ed. New York: Springer; 2006.
31. Hassanzadeh Tabrizi SA. Synthesis, characterization, and magnetic properties of $NiFe_2O_4$ nanoparticles. Journal of Particle Science and Technology. 2022;8(2):79-85.
32. Caldeira LE, Erhardt CS, Mariosi FR, Venturini J, Zampiva RY, Montedo OR, Arcaro S, Bergmann CP, Braganca SR. Correlation of synthesis parameters to the structural and magnetic properties of spinel cobalt ferrites ($CoFe_2O_4$)–an experimental and statistical study. Journal of Magnetism and Magnetic Materials. 2022;550:169128.
33. Asif M, Irshad W, Asif MI, Almufarij RS, Alanazi YM, Hassan RU, Ahmad M, Ashraf GA, Jumanazarov D, Atamurotov F. Synthesis, DFT calculations, magnetic, and high-frequency dielectric properties of nickel ferrite ($NiFe_2O_4$). Journal of Materials Science: Materials in Electronics. 2025;36(29):1-9.
34. Noreen S, Hussain A. Structural, optical, morphological and magnetic properties of $Cu_{0.25}M_{0.75}Fe_2O_4$ (M= Mn, Mg, Ni and co) ferrites for optoelectronic applications. Optical Materials. 2023;139:113797.
35. Al-Senani GM, Al-Fawzan FF, Almufarij RS, Abd-Elkader OH, Deraz NM. Biosynthesis, physicochemical and magnetic properties of inverse spinel nickel ferrite system. Crystals. 2022;12(11):1542.
36. AL-Sawafi MO, Nanakali NM, Abbasi A, Sadaka MW, Abed SH, Kadhim SA, Fini MS, Heydaryan K. Thermally

Engineered $NiFe_2O_4$ Nanoparticles via Controlled Decomposition: A High-Performance Candidate for Magnetic Hyperthermia Applications-Based Cancer Therapy. Journal of Superconductivity and Novel Magnetism. 2025;38(5):210.
37. Vahedrouz F, Alizadeh M, Bahrami A, Heidari Laybidi F. Magnetic Behavior of Co^{2+}-Doped $NiFe_2O_4$ Nanoparticles with Single-Phase Spinel Structure. Crystals. 2025;15(7):624.
38. Haneef M, Gul IH, Hussain M, Hassan I. Investigation of magnetic and dielectric properties of cobalt cubic spinel ferrite nanoparticles synthesized by CTAB-assisted co-precipitation method. Journal of Superconductivity and Novel Magnetism. 2021;34(5):1467-76.
39. Ahmad MN, Khan H, Islam L, Alnasir MH, Ahmad SN, Qureshi MT, Khan MY. Investigating nickel ferrite ($NiFe_2O_4$) nanoparticles for magnetic hyperthermia applications. J. Mater. Phys. Sci. 2023;4(1):32-45.
40. Nazari N, Golzan MM, Mabhouti K. Evaluating eddy current behavior and magnetic loss in pure and Mn/Zn-doped $NiFe_2O_4$ spinel ferrites. Scientific Reports. 2025;15(1):25169.
41. Kore EK, Kore AE, Shaikh SA, Nargundkar GP, Bandgar SS, Pawar SG, Chavan SD, Chanmal CV. Structural, magnetic, and antibacterial properties of Mn-Substituted $CoFe_2O_4$ nanoparticles synthesized via coprecipitation. Applied Physics A. 2025;131(8):613.
42. Amin KM, Eldeeb NA, Gargar Z, Mohamed IM, Elsenety M, Emara MM, Abd Elkodous M, Abouelela MM, Ibrahim PA, Ayed AA, Abdelhamid HN. Ferrite-based nanomaterials for photocatalytic CO_2 reduction: Synthesis, properties, and mechanistic insights. Journal of CO_2 Utilization. 2025;100:103175.